Sensors & Actuators: A. Physical 355 (2023) 114252

Contents lists available at ScienceDirect

Sensors and Actuators: A. Physical

journal homepage: www.journals.elsevier.com/sensors-and-actuators-a-physical

Ferrofluid electromagnetic actuators for high-fidelity haptic feedback

Nikolas Kastor [d,1], Bharat Dandu [b,1], Vedad Bassari [a], Gregory Reardon [c], Yon Visell [b,c,d,*]

[a] Department of Mechanical Engineering, University of California, Santa Barbara, 93106, CA, USA
[b] Electrical and Computer Engineering, University of California, Santa Barbara, 93106, CA, USA
[c] Media Arts and Technology, University of California, Santa Barbara, 93106, CA, USA
[d] Biological Engineering, University of California, Santa Barbara, 93106, CA, USA

ARTICLE INFO

Keywords:
Actuators
Electromagnetic
Haptics
Ferrofluid

ABSTRACT

Engineering high-fidelity haptic actuators is challenging due to the impressive tactile sensing characteristics of human skin, which possesses a wide frequency bandwidth, high spatial and temporal resolution, and large dynamic range. These attributes cannot be matched by existing haptic feedback technologies. Efficient, compact electromagnetic haptic actuators are needed in many emerging haptic systems, but their bandwidth and dynamic range are fundamentally constrained by heat transfer effects that become extremely limiting as device dimensions are decreased. Here, we present a compact actuator for delivering high-fidelity haptic feedback via an electromagnetic assembly comprising a magnetically-driven fabric-reinforced elastic membrane coupled to a ferrofluid encapsulated magnetic circuit. Using theoretical modeling, simulations, and experiments, we show how the mechanical design, magnetic circuit, and thermal design of this fingertip-sized actuator enable it to deliver sustained forces or indentations, wide-bandwidth vibrations, sustained forces of 3 Newtons, transient forces exceeding 13 Newtons. These actuators can be leveraged to supply many emerging systems and products with high fidelity haptic feedback.

1. Introduction

Haptic actuators are electronic devices for mechanically stimulating the skin in the range of human touch sensitivity. Such actuators are widely used in mobile computing devices, game controllers, wearable electronics, virtual reality interfaces, and other devices [1]. Haptic actuators are also being widely investigated for augmented and virtual reality, robotic surgical interfaces, surgical simulators, prosthetics, and other domains [2,3].

The skin, the sensory organ of touch, integrates many thousands of tactile receptors, and multiple receptor types, that enable it to capture mechanical signals over a wide frequency range, from 0 to 1000 Hz [4]. Near frequencies of 200 to 300 Hz, vibrations with amplitudes smaller than 10 nanometers can be felt, surface textures on the scale of tens of nanometers can be discriminated, and locations of light touch contact can be discriminated with millimeter precision; see [5] for a recent review discussion. The dynamic range of perceivable forces is also impressive, extending from approximately 10^{-3} to 10^{2} Newtons. No existing haptic device is capable of generating mechanical signals across the breadth of this range of frequency, spatial resolution, and dynamic range [5,6]. The large disparity between haptic perceptual abilities and the capabilities of haptic actuators has motivated substantial research efforts, but no technologies yet demonstrated can even approximately match perceptual capabilities [7–10].

Among the most common haptic technologies for stimulating the skin are electromagnetic actuators. In both commercial haptic products and in haptics research, voice-coil actuators are widely used. Examples include narrow-bandwidth linear resonant actuators and wider-bandwidth Laplace force actuators [1,8,11]. Such devices comprise an assembly including a permanent magnet (or magnets) and voice coil coupled within a casing via springs or elastic members.

Sealed inertial actuator designs are very widely used in applications. When driven, the coil produces an electromagnetic force causing the magnet to oscillate. The resulting oscillating motions are transferred to the skin (or other surface), via conservation of momentum. Such devices can be designed to be inexpensive, and are often simple to drive at low voltages with commodity electronics, similar in both respects to inexpensive loudspeakers. However, the practical bandwidth of such devices is limited to a single frequency, if driven at the mechanical resonant frequency f_0 or to frequencies strictly greater than f_0 if wider bandwidth operation is needed [12]. Consequently, the operating bandwidth of such devices is constrained, and they are furthermore unable to deliver sustained or low frequency forces (near DC) or

* Corresponding author at: Biological Engineering, University of California, Santa Barbara, 93106, CA, USA.
E-mail address: yonvisell@ucsb.edu (Y. Visell).
[1] These authors contributed equally.

https://doi.org/10.1016/j.sna.2023.114252
Received 12 October 2022; Received in revised form 5 January 2023; Accepted 14 February 2023
Available online 16 February 2023

displacements to the skin. Such stimuli are commonly felt during sustained or transient contact with familiar objects and surfaces [4].

Non-inertial electromagnetic actuators, like those reported here, can be designed to directly stimulate the skin in order to supply sustained (DC), transient, or oscillating forces or displacements. Several examples have been previously investigated [13–16]. Such actuators can furnish feedback that approximates touch sensations, such as sustained indentations of the skin like those felt when an object is touched or grasped, as well as transient or oscillating vibrations, like those felt during brief contact, or when haptically exploring a textured surface [1]. In applications, feedback supplied by such actuators can enhance or augment touch interactions with digital content or physical objects [17–20].

However, fundamental constraints arising from heat transfer limit the magnitude of forces that can be produced by compact, wide bandwidth actuators, such as are needed in many handheld or wearable haptic applications. The maximum force F that can be produced by a permanent magnet electromagnetic actuator scales as $F \propto l^2$, where l is a length scale parameter [21]. These constraints greatly limit the dynamic range of forces that can be reproduced by inertial or DC-coupled electromagnetic actuators with sizes appropriate for wearable and mobile haptics applications.

Here, we describe the design of new compact haptic actuators that are capable of supplying substantial forces or indentations to the skin, and of accurately reproducing high dynamic range tactile vibrations over the entire frequency range that is perceivable by touch. Their performance is achieved via several unique design features, including a parsimonious electromechanical design, and an efficient, ferrofluid-encapsulated electromagnetic circuit.

Ferrofluids are colloidal suspensions of paramagnetic metal nanoparticles in a carrier liquid. Ferrofluid suspensions remain stably dispersed due to the nanometer scale dimensions of the particles. Several properties of these engineered fluids make them attractive for use in high-performance electromagnetic actuator designs. First, due to its high thermal conductivity, ferrofluid aids heat transport, thus alleviating thermal limitations on performance. Second, ferrofluid is paramagnetic, thus can reduce the magnetic reluctance of electromagnetic circuits, thereby amplifying forces. Third, the rheological properties of ferrofluid can aid actuator dynamics, by lubricating motion and furnishing viscous damping. Damping is often desirable for reducing mechanical resonances, which otherwise constrain actuator bandwidth and transient performance. We analyze each of these effects, and their benefits for the actuator reported here, in later portions of this manuscript.

The aforementioned benefits have motivated prior uses of ferrofluid in high-performance loudspeakers [22,23], and in voice coil actuators for motion control, fluidic valves, vibration control [24–28]. Magnetic fluid designs (using ferrofluid or magnetorheological fluid) have recently been investigated for indirectly reproducing haptic feedback patterns [29,30].

Current generation mobile phones integrate compact electromagnetic haptic actuators. Some of these integrate small amounts of ferrofluid to lubricate motion and improve thermal heat transport. However, such commercial actuators furnish vibration feedback via movements of elastically sprung internal moving masses. Because they are inertially coupled, such actuators unable to produce sustained forces or displacements. Moreover, most such actuators use small quantities of ferrofluid, sufficient for lubrication and thermal management, because substantial resonance is beneficial for reasons of power efficiency, especially for open-loop actuation in handheld or wrist-worn devices. Driving such actuators at tactile frequencies other than the natural resonant frequency can require additional electronics and sophisticated feedback control techniques.

Other electromagnetic actuator designs can achieve greater operating bandwidths in open loop operation. This is achieved by designing the actuators to be less damped than resonant devices, which results in a lower Q factor. The Q factor also the ratio of the energy stored to the energy lost per cycle. A lower Q factor means that the actuator loses more energy per cycle, resulting in lower power efficiency compared to resonant devices. However, this trade-off can allow an actuator to operate over a wider range of frequencies without the need for feedback control electronics or techniques.

Traditional compact haptic actuators rely on vibrations produced by elastically sprung internal moving masses to furnish feedback. The vibration output of actuators operating above 0 Hz is most frequently characterized in terms of their inertial acceleration response in unloaded conditions.

The ferrofluid electromagnetic actuators presented here are also DC coupled and can be designed to operate over the entire tactile frequency range, from 0 to 1000 Hz in open loop mode. This allows them to produce sustained forces or displacements, in addition to vibrations. In addition to their wide operating bandwidth, these ferrofluid electromagnetic actuators are also compact and can be easily integrated into a variety of devices. Their performance and compact form factor make them particularly suitable for use in mobile computing and wearable haptic applications, such as augmented reality systems and handheld game controllers. They also have potential applications in the automotive industry, including use in cockpit controls, and in other consumer devices.

2. Design concept and operating principle

Our design was informed by several of the foregoing considerations. To facilitate the use of these actuators in a wide range of emerging haptic application areas, we determined that its dimensions should be comparable to those of a small handheld object, such as a marble, or comparable in size to an adult fingertip. We aimed to engineer the device to be capable of reproducing frequencies from DC (0 Hz) up to nearly 1 kHz, a range that includes both static forces with magnitudes on the order of 1 Newton (which is representative of the forces produced when feeling objects or surfaces), and higher frequency vibrations. To achieve this, we used a direct drive moving-magnet voice-coil configuration in which the surface driven by the magnet assembly is placed in contact with the skin. We designed the device to minimize mechanical resonances across this frequency range. This was aided by the damping characteristics of the encapsulated ferrofluid. Ferrofluid also improved heat transfer, alleviating thermal constraints on device performance. The range of forces that could be produced was augmented by the use of a paramagnetic core within the electromagnet. We offset the ensuing attractive force between the moving magnet and core via a magnetic bearing that was implemented via a second permanent magnet placed in series with the magnetic circuit. These features, and optimizations of the geometry and assembled configuration, together maximized the feasible dynamic range of forces and displacements that could be delivered to the skin via the actuator.

The actuator employs two axially aligned permanent neodymium magnets (parts C and J; refer to Fig. 1A for the design and part labels), which have their like poles facing each other, resulting in a static repulsive force F_{static} between them. One of the magnets is embedded within the ferromagnetic actuator housing (G), while the other is suspended at the far end of the actuator within a fiber reinforced membrane diaphragm (E). A copper coil (K) wound around a ferromagnetic core (H) is placed in the region between the two magnets, such that it contacts the embedded, fixed magnet (J) and has some clearance with the suspended, floating magnet (C). The application of current I to the coil results in additional magnetic flux through the system, which interacts with the suspended magnet to apply added electromagnetic forces $F_{em}(I)$ to it. The membrane in the annular region between the magnet and the actuator housing acts as a spring that provides a restoring force $F_{mem}(\delta)$ with imposed displacements δ, and can thus return the moving mass assembly to a zero position when the currents are turned off. To reduce the reluctance of the magnetic circuit, a small top plate (D) is introduced into the moving mass assembly. A linear

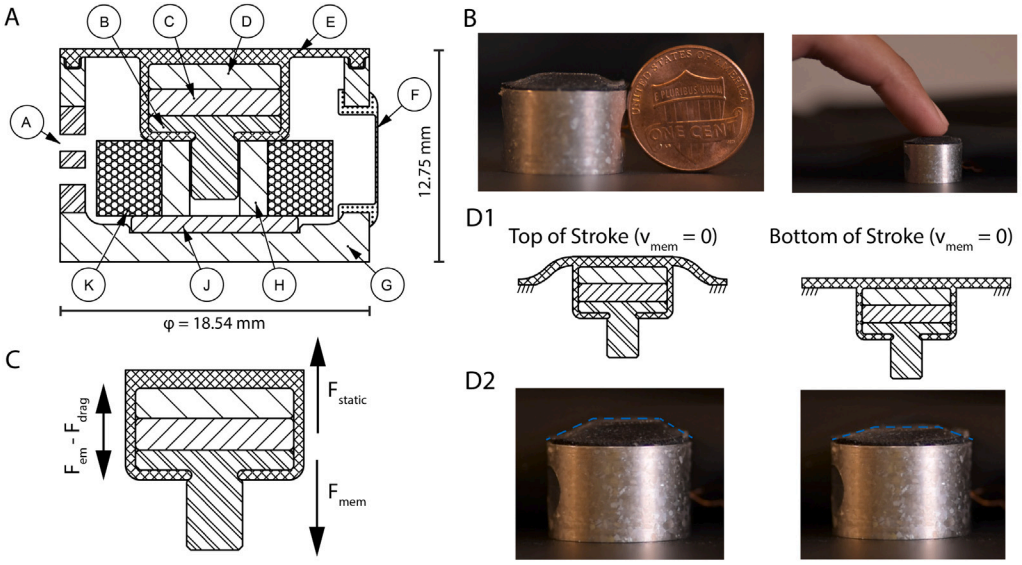

Fig. 1. The compact fluidic EM haptic actuator design resulted from our theoretical modeling, numerical simulations, analyses, and fabrication process. (A) Schematic drawing of the actuator. Cross-section with the following components. A: Filling and wiring ports. B: Piston-cylinder bearing. C: Permanent magnet. D: High magnetic permeability plate. E: Fiber-reinforced membrane diaphragm. F: Fluid displacement feature (optional). G: High magnetic permeability housing. H: High magnetic permeability electromagnet core. J: Fixed permanent magnet. K: Copper electromagnet coil. Dimensions of the actuator are listed. (B) Images of constructed actuator. One cent coin to scale. (C) Free body diagram of the moving mass of the actuator. F_{static} denotes the net repulsive forces due to the magnetic components. F_{mem} denotes the restoring force of the membrane. F_{em} and F_{drag} are the forces due to the current through the coil and the viscous drag respectively. (D1) Diagrams showing the moving mass at the top and bottom of its stroke. (D2) Images highlighting the top and bottom of the stroke of the constructed actuator, when it is driven by a 1 A rms 0.5 Hz sinusoidal signal.

bearing comprising a miniature shaft within the core, and bearing (B) is introduced to limit displacements in the radial direction and out-of-plane rotations. This feature could introduce additional drag forces F_{drag}, which are minimized in our design through the use of a hollow bearing shaft. The actuator is filled with ferrofluid to further improve the magnetic performance, aid thermal performance, as well as to introduce damping to the system, thereby limiting the impact of resonance. A picture of the constructed prototype with no input current shown in Fig. 1B.

The moving mass of the actuator is designed to directly contact the skin. With the moving magnet assembly produces a forces that satisfy, in quasi-static conditions, $F_{act}(I) = F_{em}(I) + F_{static} - F_{mem} - F_{drag}$.

The magnetic bearing results from repulsive forces between the magnets. The magnet geometries ensured that the nominal position of the moving magnet was at the center of the range of its motion even when lightly loaded. In the absence of external loading of the moving magnet, the moving magnet displaces until the restoring force of the membrane is balanced by the those due to the electromagnet, membrane, and magnetic bearing. The clearance specified in the design between the moving mass assembly and the core serves as a hard limit to the displacement at the bottom of the stroke of motion, when large negative currents are driven through the coil (values reflecting the performance of our device are reported below). The displacement at the top of the stroke is constrained, at the largest excursions, by the membrane hyperelasticity (Fig. 1D). We empirically identified the approximately linear range of motion as a function of current within the displacement extremes.

3. Electromagnetic modeling

The forces generated from this electromagnetic actuator design are determined primarily by the resultant forces on the moving magnet assembly, which we model both analytically and with numerical simulations.

3.1. Analytical modeling

The resultant force on the moving magnet can be decomposed into the static repulsive force between the two permanent magnets and the electromagnetic force between the coil and the suspended magnet element. Each of these were modeled separately.

The forces on a permanent magnet with magnetization **M** in an external magnetic field **B** can be derived by considering a differential volume inside it with a magnetic moment $\mathbf{m} = \mathbf{M}dV$. The total force **F** is computed using the electric current loop model in the absence of electrical currents within the magnetic volume, and integrating the differential forces [31,32] -

$$\mathbf{F} = \int_V \nabla(\mathbf{m} \cdot \mathbf{B}) dV \tag{1}$$

The actual forces that are realized depend on the geometry of the system. To gain qualitative insight about the system, in a first analysis, we first neglected the effect of the ferromagnetic components (top plate, housing and core; parts D, G and H in Fig. 1). We obtained an expression for the axial force $F_{z,mm}$ between the two coaxial cylindrical magnets (i.e. the fixed and suspended magnet) by performing the elliptic integrals arising from the remaining geometry, using a low-order approximation for the Bessel function terms that arise, which is accurate in the limit that the intermagnet distance is large compared to the magnet dimensions [33]. Computation yields

$$F_{z,mm} \approx \frac{1}{4}\pi\mu_0 M^2 r_m^4 \sum_{i,j=0}^{1} \frac{(-1)^{i+j}}{(d_{\mathrm{mm}} + it_1 + jt_2)^2} \tag{2}$$

Here, $M = B_0/\mu_0$ is the saturation magnetization of the permanent magnets, B_0 is the residual flux density d_{mm} is the distance between the poles, r_m is the common radius of the magnets, and t_1, t_2 are the heights of the individual magnets. In the remainder, we omit the subscript z and consider all forces to be in the axial direction unless otherwise noted.

To compute the axial force between the electromagnetic coil and the suspended magnet F_{em}, we used an equivalent inductor representation of the permanent magnet. We obtain an expression for the

force between the two by computing their mutual inductance, under the assumption that the magnet is smaller than the coil and the field lines from the coil are nearly parallel to the magnetic moment of the magnet [34]. This yielded

$$F_{em} \approx \frac{\mu_0 n_s I_s M \pi r_m^2}{2} \times \left[\frac{d_{\mathrm{mc}} + t_s + t_m}{\sqrt{(d_{\mathrm{mc}} + t_s + t_m)^2 + r_s^2}} - \frac{d_{\mathrm{mc}} + t_s}{\sqrt{(d_{\mathrm{mc}} + t_s)^2 + r_s^2}} - \frac{d_{\mathrm{mc}} + t_m}{\sqrt{(d_{\mathrm{mc}} + t_m)^2 + r_s^2}} + \frac{d_{\mathrm{mc}}}{\sqrt{d_{\mathrm{mc}}^2 + r_s^2}} \right] \quad (3)$$

where n_s is the number of turns per unit length of the coil, I_s is the current, r_s, t_s are the radius and length of the coil respectively, t_m is the height of the magnet, and d_{mc} is the axial distance between the closest ends of the coil and magnet. If axial symmetry is maintained, the net torque on the suspended magnet due to the magnetic field of either the fixed magnet or the electromagnetic coil is zero.

We examined the solutions using geometrical parameters that matched those of the fabricated actuator (described in later sections). The analytical model provides a static force F_{mm} of 0.59 N when the pole to pole distance d_{mm} is 7 mm, with $d_{\mathrm{mc}} = d_{\mathrm{mm}} - t_s = 2.5$ mm. The resulting electromagnetic force F_{em} of 0.21 N per Ampere.

The reluctance of the designed actuator was further reduced beyond that of this free-space description through addition of ferrofluid and the use of a high magnetic permeability alloy for the core, cylindrical shield and cap. Together, these reduce the magnetic reluctance of the circuit, increasing flux density **B**, and increase the magnitude of force that are produced. These additions alter the magnetic flux paths, which travel along paths that are more curved than in free space. This yields a small accompanying reduction in force due to the dependence of force on $\mathbf{m} \cdot \mathbf{B}$ in Eq. (1). The presence of the high permeability alloy also introduces an additional interaction force F_{int} between the magnets and the alloy, including prominent forces between the suspended magnet and the core, and smaller forces between the fixed (lower) magnet and top plate, and between the suspended magnet and the cylindrical shield. This alters the static repulsive force on the moving mass, $F_{static} = F_{mm} - F_{int}$. The alloy materials also affect the current-dependent electromagnetic force. An analytical expression for F_{int} is difficult to compute in general, but the small cross-sectional area of the core relative to the flux paths of the magnet ensures that the actuator can be expected to perform as designed. We quantitatively analyzed these effects using numerical simulations, from which we obtained values of F_{static} and F_{em} as driving current is varied, and used the results to optimize the geometry of the actuator.

3.2. Numerical simulations

We simulated the forces generated by the actuator using multiphysics finite element analysis (FEA; COMSOL AB, Stockholm, Sweden). We developed an axisymmetric model of the actuator, and evaluated the axial magnetic force. The geometry and materials were specified to match the fabricated device (Section 6), with the dimensions as shown in Fig. 1A. The coil was modeled as a homogenized multi-turn structure. The ferromagnetic materials were configured as Nickel Steel Permalloy NGO, as defined within the COMSOL material library. The ferromagnetic materials were modeled with a BH curve relation. The ferrofluid was modeled as a homogeneous material with a relative permeability μ_r of 2, consistent with reported values. Representative surface plots of the magnetic flux densities through the cross-section of the actuator are shown in Fig. 2A.

When the electromagnet was not driven, the net force, $F_{static} = F_{mm} - F_{int}$, on the moving magnet was due to the opposing forces F_{mm} due to the magnetic bearing formed from the oppositely poled permanent magnets and F_{int} due to the attraction between the moving magnet and the core. The simulations predict that F_{static} decreases monotonically with the magnet–magnet distance d_{mm} (Fig. 2B). The relationship was approximately linear for distances $6 < d_{\mathrm{mm}} < 7.5$ mm, attaining a value of 1.45 N for $d_{\mathrm{mm}} = 7$ mm.

With d_{mc} held constant, the electromagnetic force on the moving mass F_{em} increased with the current (Fig. 2C). The relationship was nearly linear, notwithstanding potential effects of flux saturation within the core, with a slope of 0.87 N/A for $d_{\mathrm{mc}} = 2.5$ mm. This force was nearly four times larger than predicted from our simplified analytical model, highlighting the decrease in reluctance of the magnetic circuit achieved through the use of the ferromagnetic elements. We also simulated forces for a configuration in which the ferrofluid was replaced with air. This configuration yielded smaller forces of 0.62 N/A. Thus, a 35% increase in forces was produced due to the greater magnetic permeability of the integrated ferrofluid.

To validate the analytical models, we performed simulations where we specified the physics model of all materials to utilize a relative permeability equation, and artificially set the magnetic permeability of the ferromagnetic components and ferrofluid to be 1. The modified FEA simulations yielded $F_{mm} = 0.32$ N, and $F_{em} = 0.2$ N/A. The electromagnetic output force, F_{em} obtained from the simulations was thus in excellent agreement with the analytical model. The analytical model did, however, overestimate by 85% the magnitude of the static repulsive force F_{mm} between the fixed and floating magnet, which cause the floating magnet to levitate, when compared to simulations. We hypothesize this to be due to the far-field approximations involved in the derivation.

To investigate effects of lateral displacement of the moving magnet, we simulated configurations in which the magnet center was offset from the axis of the electromagnet. While the magnet position is constrained, in practice, by the membrane, the simulation revealed that it is located at an unstable equilibrium in the radial direction. A radial offset of 1 mm introduced a radial force F_r of 1.3 N, and also yielded a net torque of 2×10^{-4} Nm. Such effects can yield ancillary linear or torsional oscillations in the absence of constraining features. We revised our design to minimize such effects via a guide bearing that was formed by extending an aluminum shaft from the magnet into a hollow region of the core (Part B in Fig. 1A). The shaft and bearing did not modify the electromagnetic performance, and only modestly affected the dynamics of the system, due to the lubricating effects of the ferrofluid.

4. Mechanical modeling

We constructed an analytical model capturing the static and dynamic mechanical behavior of the actuator. The actuator performance depends on several factors, including the membrane elasticity, inertia of the moving elements, and dissipative forces caused by the viscous fluid within the actuator.

4.1. Static forces

The forces acting on the moving magnet assembly include the force F_{em} produced by the electromagnet, the repulsive force F_{static} between the permanent magnets, the force F_{mem} due to membrane deformation, and the viscous force F_{drag} due to the encapsulated fluid. A free body diagram of forces on the moving mass is shown in Fig. 1C.

When the coil is not energized, if the system is in static equilibrium, then $F_{static} - F_{mem} = 0$ and $F_{em} = F_{drag} = 0$. Applying an additional static load force F_{load} to the surface of the moving magnet assembly will displace it from this equilibrium. For sufficiently small static load forces, a new equilibrium is reached, satisfying

$$F_{static} - F_{mem} = F_{load} - F_{em} \quad (4)$$

The force due to gravity is far smaller, due to the low mass of the moving magnet assembly, and thus may be neglected.

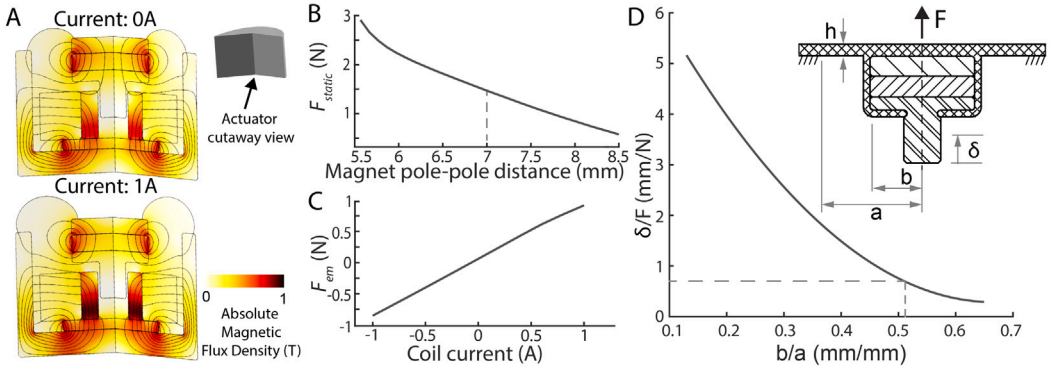

Fig. 2. Modeling and simulation results utilized in the design of the actuator. (A) Numerical predictions of magnetic flux densities within the actuator for varying current levels within its operating range. When driven at a DC current of 1 A, the ferromagnetic material in the core approaches its magnetic saturation. (B) The static repulsive force experienced by the moving magnet F_{static} decreases monotonically with the magnet–magnet distance. When coupled with the restoring force of the membrane, the representative magnet–magnet distance d_{mm} equals 7 mm for the moving mass in static equilibrium. (C) The scaling of electromagnetic force F_{em} with current is approximately linear with a slope of 0.87 N/A. The scaling is computed to be sub-linear at large positive currents once magnetic saturation is reached. (D) A plot of the deflection at the center of the diaphragm δ is shown as a function of force produced by the magnet assembly F, for $h = 0.5$ mm. The membrane performance can be optimized by varying dimensions a, b, and h. For the designed dimensions of the actuator, the predicted stiffness value is 1.25 N/mm.

4.2. Membrane model

The actuator is designed to accommodate application-dependent pre-loading of the membrane and mass via fluidic pressure or external forces. We omit this effect in a first analysis. Thus, the membrane displaces by an amount δ such that the membrane restoring force, F_{mem}, is equal to the net force exerted on the magnet by the electromagnetic circuit to reach static equilibrium.

4.2.1. Material mechanics

We adopted a linear material model for the membrane, which is reasonable because of the in-plane membrane strain is constrained to be small, due to the fiber reinforcement. In principle, because the membrane is a fiber-reinforced elastomer, models of Kelvin–Voigt or Helmholtz types would be appropriate mechanical models. However, manufacturing tolerances and unknown parameters governing the fiber alignment and concentricity of the assembly are challenging to obtain for laboratory produced devices such as ours, for which manufacturing tolerances are substantial. Additionally, the material properties of the elastomer matrix of the membrane can vary modestly from batch-to-batch. Thus, we adopted a simpler homogenized model of the elastomer membrane mechanics. We obtained values for the linear elastic modulus $E = 11.4$ MPa and the Poisson ratio $\nu = 0.5$ via laboratory tensile testing.

4.2.2. Membrane deformation

The geometry of the membrane was determined analytically for a circular membrane with a rigid center and a force acting at the center along the axis (Fig. 2D) [35]. The maximum deflection δ at the center of the membrane is given by

$$\delta = \frac{Fa^2}{Eh^3}\frac{3(1-\nu^2)}{\pi}\frac{(a/b)^2-1}{4(a/b)^2} - \frac{\log(a/b)^2}{(a/b)^2-1} \tag{5}$$

Where F is the net force on the moving magnet, E and ν are the elastic modulus and Poisson's ratio of the membrane material respectively, and a, b, and h are geometric dimensions shown in Fig. 2D. An approximation for the effective spring constant of the membrane can be computed from Eq. (5) as $k_{\text{eff}} = dF/d\delta$.

4.3. Viscous effects

The encapsulated ferrofluid improves thermal transport and reduces magnetic reluctance of the electromagnetic circuit, thus amplifying forces, but also influences the dynamics. Viscous ferrofluid damping reduces the Q-factor of mechanical resonances in the system, and thus augments the usable frequency bandwidth, which, in resonant designs, can be constrained by high-Q resonances [12,36].

A full fluid dynamics description of ferrofluid damping effects would be beyond the scope of the present contribution. A lumped parameter description can be obtained by regarding the combination of the guide shaft bearing and moving assembly (Fig. 1C) as comprising a dashpot, yielding a force

$$F_{drag} = -c\frac{dz}{dt} \tag{6}$$

Here, $z(t)$ is the displacement of the moving mass attached to the diaphragm, and c is the effective damping coefficient. The damping coefficient reflects contributions of shear stress due to boundary hydrodynamic lubrication along the sliding bearing interface and the stagnation pressure due to the motion of the leading surface of the guide shaft. After integrating each contribution over the respective surface and summing them, one obtains

$$c = \frac{3\pi L\mu D^3}{4d^3}(1 + 2d/D) \tag{7}$$

where d is the clearance gap, D is the guide shaft diameter, L the bearing length, and μ the dynamic fluid viscosity.

Using the parameter values describing our fabricated ferrofluid device (Section 6.2), Eq. (7) yields a damping coefficient of approximately $c = 9.8$ Ns/m. In contrast, if the same actuator is filled with air rather than ferrofluid, $c = 1.2 \times 10^{-3}$ Ns/m, which is four orders of magnitude smaller.

4.4. Dynamic forces

The motion of the unloaded driven actuator magnet can be modeled as a damped harmonic oscillator with a driving force $F_{em}(t)$ generated by the electromagnetic circuit,

$$m\frac{d^2z}{dt^2} = F_{em}(t) - c\frac{dz}{dt} - kz \tag{8}$$

where z and m are respectively the normal displacement and mass of the moving mass element (bearing, moving magnet, and top plate; parts B, C and D in Fig. 1), c is the damping coefficient (Eq. (7)), and k is the stiffness of the membrane (Section 4.2.2).

The solution to (8) is readily obtained via Fourier transform:

$$\hat{z}(\omega) = \frac{\hat{F}_{em}(\omega)(m(\omega_0^2-\omega^2) - jc\omega)}{m^2(\omega^2-\omega_0^2)^2 + c^2\omega^2} \tag{9}$$

where the undamped ($c = 0$) natural frequency of the system is $\omega_0 = \sqrt{k/m}$. For sinusoidal driving signals, $F_{em} = A\cos(\omega t)$, the solution is:

$$z(t) = \frac{A}{\sqrt{m^2(\omega^2 - \omega_0^2)^2 + c^2\omega^2}}\cos(\omega t - \phi)$$
$$\phi = \arctan\left(\frac{\omega c}{m(\omega^2 - \omega_0^2)}\right) \tag{10}$$

When $c/m \gg 1$, the system is dominated by damping, and resonance effects are thus minimized. Such a system exhibits several properties that are desirable for a haptic actuator, with the acceleration d^2z/dt^2 being uniform across frequencies, and the system possessing a linear phase response.

4.5. Geometry optimization

The results and insights from the electromagnetic and mechanical modeling were used to optimize the geometry of our fabricated device, as shown in Fig. 1. The actuator dimensions were specified in order to allow it to supply haptic feedback to the human fingertip. The diameter of the actuator was selected to be 18.5 mm, which is slightly wider than the average width of a typical adult index finger.

The diaphragm thickness h of the membrane could only be varied in manufacturing by 0.5 mm increments, due to the fixed layer thickness of the fabric reinforcement. In order to maximize the displacement, the minimum thickness of 0.5 mm was used. Without the reinforcement layer, lateral forces produced by the magnet assembly location would fall outside of the minimum concentricity tolerance, thus would cause the membrane to buckle or the magnet assembly to rotate out-of-plane.

The actuator housing dimension a was selected to be as 7.75 mm based on manufacturing and electro-mechanical considerations. The dimension b was selected to yield a membrane stiffness of approximately 1 N/mm, to ensure deformations within the displacement limits of the bearing, upon the application of forces. Based on this constraint and the available dimensions of commercially available rare-earth magnets, we selected the radius of all elements within the moving mass assembly b to be 3.97 mm. This resulted in a predicted stiffness of $k_{\text{eff}} = 1.25$ N/mm 2.

The fixed magnet placed at the bottom of the actuator was selected to be wide and low profile, to minimize the magnetic reluctance it imposes in the flux path.

The coil was wound with a wire of conductor diameter 0.255 mm (30 AWG), which imposes a continuous operation current limitation of 0.86 A. The bearing dimensions, such as the clearance gap and piston length (Section 4.3), were specified based on machining and fluid transport constraints.

We then considered the length of the core/coil assembly, the outer diameter of the core, the thickness of the moving magnet, the thickness of the top plate, and the distance between the moving magnet and core as free parameters, and optimized the geometry by running parameter sweeps with step sizes of .25 mm within our FEA numerical models. We identified the configuration that produces the largest electromagnetic force F_{em}. We also imposed an additional constraint during this process to verify that during regular operation within current limits, the sum $F_{static} + F_{em}$ is always positive. This ensured that the force never turned attractive during regular operating conditions, which would have caused the moving mass to adhere to the ferromagnetic core and introduce significant non-linearities.

5. Thermal modeling

The robustness of the proposed actuator depends on its the thermal properties of the constituent materials and the electromechanical design. Compact electromagnetic actuators produce substantial heat from resistive and inductive heating. Due to their small mass, heat densities can be large, while the small exterior surface area constrains cooling. Thus, thermal considerations often constrain the performance of compact electromagnetic actuators. Absent other design features, such as active cooling, the maximum force F that can me produced by such actuators scales as $F \propto l^2$, where l is a dimensional length scale [21].

5.1. Thermal constraints on performance

We identified three thermal constraints arising from typical failure modes. First, high temperatures within the coil can melt, shorting the coil. Second, if the permanent magnets are heated above the Curie temperature of the material then demagnetization will result. Third, if the temperature of the magnetic circuit exceeds the Curie temperature of the paramagnetic alloy (Permalloy-80), the magnetic permeability of the material, and thus the forces that can be produced, will be greatly reduced. We obtained operating temperature limits from these criteria based on properties of the materials involved (see Table 1).

5.2. Heat transport analyses

Heat that is produced resistively and inductively in our design is transported to the device exterior surfaces via solid components and ferrofluid, where it is transferred to the surrounding environment. Thermal transport within the actuator is governed by a heat equation:

$$\rho C_p \frac{\delta T}{\delta t} + \rho C_p \mathbf{u}\cdot\nabla T + \nabla\cdot\mathbf{q} = Q + Q_{ted} \tag{11}$$

where T is temperature, t is time, ρ is the material density, C_p is the specific heat at constant pressure, $\mathbf{u}$ is translational velocity vector, $\mathbf{q}$ is the conductive flux, Q is the heat received from additional sources, and Q_{ted} is the heat dissipated through mechanical stress.

In our device, heat that is generated resistively in the coil (which is bonded with a thermally conductive epoxy) is transferred to the aluminum linear bearing (item H in Fig. 1 A) and the encapsulated ferrofluid. The aluminum bearing transfers substantial heat to the fixed permanent magnet (item J in Fig. 1 A). The heat capacity of ferrofluid is far higher than air. Thus, the encapsulated ferrofluid enhances heat transfer, and reduces internal temperatures.

We simulated transient heat transfer using axisymmetric finite element analysis (COMSOL Multiphysics, COMSOL Inc.) based on the geometry and materials of our device. We simulated two minutes of continuous operation, which is substantially longer than such haptic actuators are continuously driven. We performed fully time-dependent simulations because we determined that the device's configuration prevents it from reaching steady-state temperatures over the simulation time scale.

The heat transfer models used the material properties listed in Table 1. To account for the range of commercially available materials, we created two simulations to represent best and worst-case failure scenarios. We modeled the electromagnetic coil as a single material to eliminate the computational cost associated with its detailed geometry. To do so, we established an equivalent value of thermal conductivity for the coil using results from an auxiliary simulation [37]. The effective coil conductance was obtained from the equation

$$G_{cond-rad} = \frac{\dot{Q}}{T_{max} - T_{wall}}, \tag{12}$$

using values obtained from an auxiliary simulation of the coil alone. Here, $G_{cond-rad}$ is the radial conductance of the coil, $\dot{Q}$ is dissipated heat flux, T_{max} is the maximum temperature domain, and T_{wall} is the temperature imposed at the coil's upper edge. The equivalent radial conductivity, λ_{eq}^r, was then obtained as

$$\lambda_{eq}^r = \frac{G_{cond-rad}\cdot e_r}{S_r} \tag{13}$$

where S_r and e_r are the coil width and half-length, respectively. The value of the specific heat capacity of the coil was set equal to that of the wire insulator since the insulator was the limiting factor.

Table 1
Material properties used in the thermal models of the actuator.

Material	Heat capacity ($\frac{J}{kgK}$)		Thermal conductivity ($\frac{W}{mK}$)		Density ($\frac{kg}{m^3}$)		References
	Maximum	Minimum	Maximum	Minimum	Maximum	Minimum	
Permalloy 80	502.42	494.34	34.61	19.66	9992.45	8740.00	[39] [40]
N50 Neodymium Magnet	502.42	460.55	8.96	6.16	7600.00	7500.00	[41] [42]
Thermal Epoxy	1100	1038.25	5.76	0.17	1150.00	1150.00	[43] [44]
Wire Insulator	2300.00	1090.00	0.35	0.15	1540.00	1380.00	[45]
Ferrofluid	4000.00	1500.00	0.80	0.60	1200.00	1000.00	[46] [47]

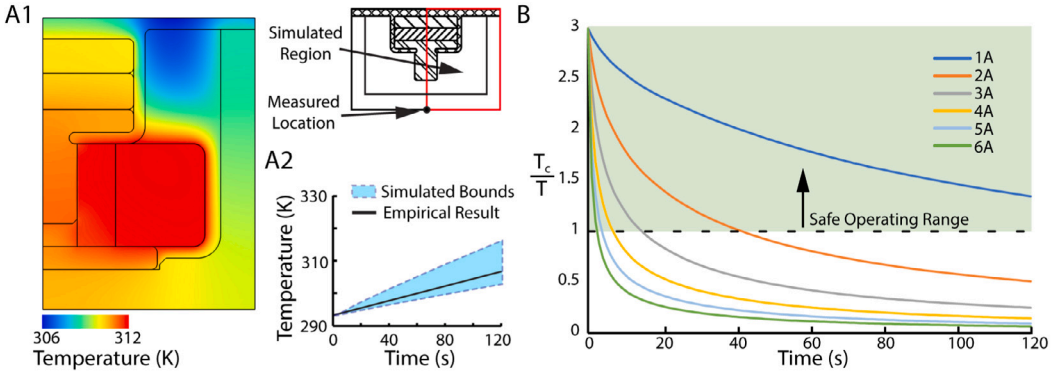

Fig. 3. Representative results from thermal simulations and experiments. (A1) Temperature after 120 s of operation at I = 1 A. (A2) Numerical and experimental temperature at actuator base vs time, I = 1 A. (B) Ratio of the critical temperature of demagnetization (T_c) to the maximum temperature (T) at varying input currents plotted after 120 s of continuous operation. The sealed configuration means that the steady-state regime takes longer to set in; a time limit of 120 s of continuous use is implemented as a reasonable sustained operational condition in a haptics experimental setting. The results suggests that 1 A of current can be driven through the actuator for more than two minutes, and larger current values can be safely used for shorter intervals.

We modeled inductive heating using an effective model of eddy current losses in wires [38], and analyzed the results in order to determine that the heat generated within the bearing and the ferromagnetic components as fabricated was less than 100 mW at all frequencies below 1000 Hz, which is the highest frequency at which such haptic actuators are driven (because higher frequencies cannot be felt via touch). Based on this analysis, we determined that inductive heating was far smaller than Joule heating in the coil. We thus neglected inductive heating in the simulations. Subsequent simulations thus accounted for thermal transport and resistive heat generation in the coil. We modeled natural external convection using Nusselt-number correlations for flat plates. We accounted for thermal contact resistances at the metallic interfaces using representative values for the roughness of machined surfaces, with an interstitial air layer applied at exposed surfaces.

We conducted these simulations using DC driving current values from 0 to 6 A, and repeated the simulations for configurations with and without the ferrofluid. Based on the results, we determined that thermal failure due to the demagnetization of the neodymium magnets was far more likely than the other modes. We further analyzed this failure condition in simulations. Representative results from the configuration with ferrofluid are included in Fig. 3. We used the ratio of the critical temperature of demagnetization (T_c) to the maximum temperature (T) to quantify thermal failure, such that a temperature ratio smaller than one indicates potential failure. The simulations predict that at 1 A of input current (intended operational condition), no failure should occur within 2 min of continuous usage. The device is capable of handling greater currents over progressively shorter intervals of time (Fig. 3B). Finally, comparing simulated temperatures to empirical results indicates that the simulations were effective in predicting the thermal performance of the device (Fig. 3A2). Together, these results indicate that the actuator design facilitates a wide usable operating regime within thermal constraints, and in conservative conditions of use.

6. Fabrication

The materials used for the prototype actuator were all chosen to meet specified requirements and optimize the performance, as described below. We then present the steps used for fabrication of the actuator. All parts are labeled as in Fig. 1.

6.1. Material selection

Fiber-reinforced silicone membrane (part E): Ecoflex 00-30 platinum cured silicone was chosen because of its durability and similar softness to human skin [48]. While the silicone provides a desirable mechanical response, it is capable of many hundreds of percent strain. With the translation of the moving mass being unconstrained, the force experienced by the permanent magnet could displace the bearing out of the shaft and even rupture the membrane. A 4-way stretch knit fabric was added to reinforce the membrane and limit its displacement. During the assembly process the fabric reinforcing layer is embedded in the silicone matrix as detailed in Section 6.2.

The magnetic circuit components (parts D, H, and G) were fabricated from an alloy designed for high-performance magnetic applications (Permalloy 80, ESPI Metals, Ashland, OR; 80% nickel, 4.4% molybdenum, 15.6% iron). These parts were machined from billet stock. They were subsequently annealed in accordance with ASTM A753 for Type 4 materials. The equipment available could not produce the 'dry hydrogen' atmosphere specified, however we were able to heat treat the material at 1150 C and quench at 300 C per hour with flowing hydrogen. As a result, the magnetic saturation of the alloy increased by 8% to ≈0.9 T, as measured by a SQUID magnetometer (MPMS, Quantum Design, San Diego, CA). The permanent magnets (parts C and J) were NdFeB rare earth magnets sourced from commercial vendors (D51-N52, KJMagnetics, Pipersville, PA; and D1058, SuperMagnetMan, Pelham, AL for magnets C and J respectively). The linear bearing (part

B) was critical for motion alignment and damping. It was fabricated from 2024 aluminum, minimizing the weight of the moving mass.

Since the volume in which the (incompressible) ferrofluid was encapsulated could deform only through membrane motion, one could question whether the associated constraints on fluid motion would affect the actuator dynamics. To investigate this, we designed a port feature that accommodated fluid displacement during actuation via a variable length elastic reservoir (part F), implemented via a thin silicone tube ($\Phi_{ID} = 3$ mm) ported to the side of the actuator (Fig. 6A). Since the results revealed effects of porting to be negligible, in other configurations of the actuator, the port (part F) is sealed with Ecoflex 00-30 polymer.

6.2. Fabrication

All of the metal components were fabricated from billet stock using standard machining and turning methods. The nickel alloy parts were subsequently annealed as described in the previous section. The core (part H) was sent to a coil fabricator to accurately wind the electromagnet coil (part K). The coil winding approximated optimal hexagonal packing, within manufacturing constraints, and was wound onto the annular core feature. The latter also furnished an alignment feature for the upper magnet in the diaphragm by locating part B, and provided the cylinder feature for the dashpot made from parts B and H.

The fabrication process involved four key steps (Fig. 4):

(A) Parts D, C, and B are assembled in a stack and added to a mold with the fiber reinforcing fabric laid on top. The assembly is then encapsulated with Ecoflex 00-30.
(B) The wire and filling port A, and fluid displacement feature F are added to the housing G. The lower permanent magnet J sticks to a shallow cavity in the housing G. The electromagnet coil assembly (parts H and K) is stuck to the top surface of the magnet and roughly centered. The wires from the electromagnet are passed through the wire outlet in A.
(C) Sub-assemblies described in steps (A) and (B) are placed in an alignment fixture, and a bead of room temperature vulcanizing silicone (RTV) is applied to the sealing surface. The fixture then marries and clamps the final assembly. During this process the aluminum piston fits into and concentrically locates the electromagnet core.
(D) Once the RTV is cured, the final assembly is removed and filled with ferrofluid. The tube comprising the fluid displacement feature is finally clamped away from the actuator to seal the system. Measurements later revealed effects of bulk fluid displacement to be negligible, so in other configurations we seal the port (part F) with Ecoflex 00-30 polymer (Section 7)

7. Characterization

To evaluate the performance of the constructed actuator, we performed dynamic mechanics and thermal characterizations. The dynamic mechanical performance was studied through transfer function, step response, and discrete sinusoid measurements. The quasi-static forces produced in an isometric configuration were also characterized in moving operation. Thermal characteristics of the actuator were measured by recording the time-dependent temperature during steady state operation.

7.1. Apparatus and procedure

The actuator was mounted in a fixture and bolted to an optical table to reduce ambient vibrations. Measurements of the actuators performance were recorded via laser doppler vibrometer and force transducer, which were also mounted to the optical table. A laboratory amplifier (PA-138, Labworks Inc., Costa Mesa, CA) and custom electronics were used to deliver specified current signals to the actuator. Current and voltage drive signals were monitored. Measurements were taken with a data acquisition system (USB-6211, National Instruments, Austin TX) controlled by a computer.

The unloaded dynamic response of the ferrofluid and air-filled actuators were characterized with a 1-axis non contact laser doppler vibrometer (PDV-100, Polytec Inc., Irvine, CA). Retro-reflective tape was attached to the center of the moving mass, which served as the position at which measurements were taken. Frequency response measurements were captured under voltage control (1–1000 Hz sinusoidal sweep, 10 s, 5 repetitions) at an array of driving amplitudes (0.125, 0.25, 0.5, 0.75, 1, 1.25, and 2.5 V). Because the frequency responses varied little between amplitudes (<0.8 dB), we averaged all measurements to obtain the voltage-specific acceleration frequency response of the actuator. We measured the step response of the actuator using current step signals with amplitudes of 0.1, 0.2, 0.4, 0.6, 0.8, and 1 A. We also characterized the actuator response to sinusoidal driving signals (20 discrete frequencies logarithmically spaced, 5 to 1000 Hz, 5 s, 5 repetitions) with amplitudes of 0.25, 0.5 and 1 A. We measured peak-to-peak displacements and computed total harmonic distortion (THD) at each frequency.

The electromagnetic force output F_{em} of the actuator was characterized at different operating displacements, using a 6-axis force–torque transducer (Nano17 F/T Sensor, ATI Industrial Automation, Apex, NC). In order to eliminate any magnetic interactions between the actuator and transducer, and to reduce the contact condition to a point load, a 2.5 cm custom cylindrical probe with a hemispherical tip was 3D-printed and fitted to the force transducer. Force was measured as the actuator was driven with each of several DC currents, which ranged from −1 A to 1 A DC in 0.2 A increments. Each measurement was repeated 3 times, with the actuator permitted to cool between measurements. The procedure was repeated at each of 3 different preload displacements that varied by 0.5 mm across the motion range of the actuator, as measured via a laser displacement sensor (IL-1000, Keyence Corporation, Itasca, IL; resolution: 10 μm).

To experimentally characterize the thermal performance of the actuator, a K-type thermocouple was affixed to the bottom of the canister with tape, and thermal measurements were taken with a digital thermometer (Fluke 52 II, Fluke Corporation, Everett, WA). The actuator was driven with a 1 A DC current for 2 min. Temperatures were recorded with a sampling period of 5 s in each of two experimental trials per actuator. For these measurements, the actuator was enclosed in a cylindrical ABS fixture. Due to the insulating effects of this fixture, which inhibited radiative heat transfer from the exterior surfaces, these measurements yielded a conservative characterization of thermal performance. In applications, one would avoid introducing such an insulating enclosure.

In haptic applications of compact actuators, transient performance is more important than steady state operation, since users are typically supplied with feedback that is brief in duration [1]. To illustrate the ability of this actuator to reproduce transient signals over a large dynamic range, we measured forces produced as the actuator was driven via short (10 ms) high amplitude current pulses, whose amplitudes ranged from 5 A to 35 A in steps of 10 A. A further pulse of 38 A was the largest that could be reproduced by the laboratory power amplifier.

To investigate any influence of the volume constraint arising from encapsulation of the ferrofluid on the actuator dynamics, we also measured unloaded dynamic responses of the actuator for different length elastic tube reservoirs.

7.2. Results

The electrical impedance of the ferrofluid actuator is dominated by its resistance, 2.7 Ω, and inductance, 1 mH. Thus, the impedance is in a range that can be driven by commodity amplifiers like those used

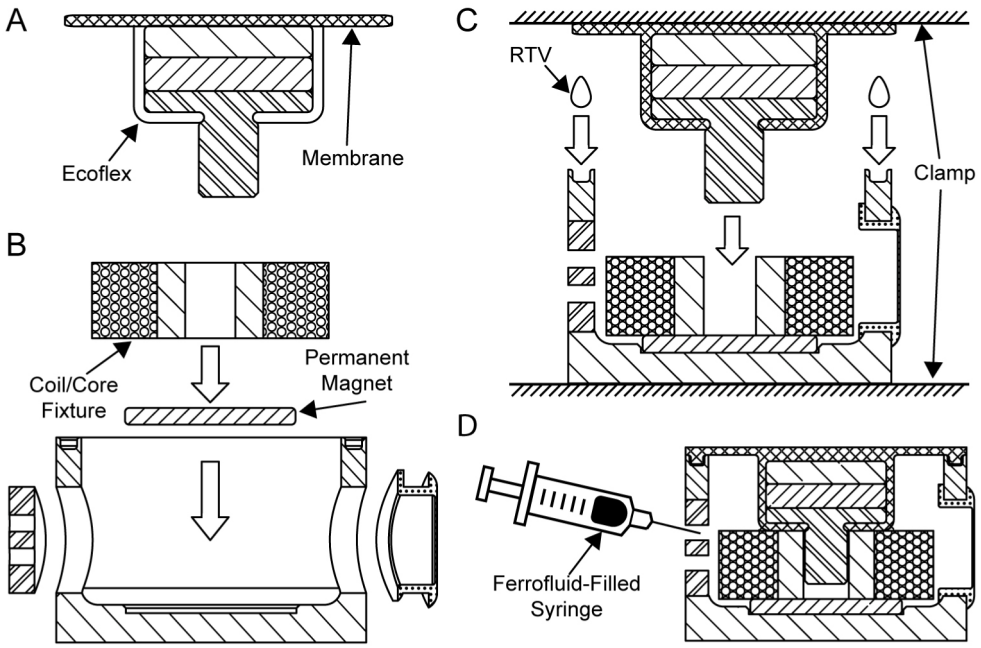

Fig. 4. The fabrication process as described in Section 6.2.

in mobile devices. The R-L inductive load of the actuator has a 3 dB point of 500 Hz; for a fixed voltage amplitude, current decreases by 6 dB per octave above 500 Hz. This behavior is appropriate for haptic actuators, since human tactile sensitivity decreases rapidly as frequency increases above 500 Hz [4]. At DC and low frequencies, supplying the actuator with 1 A RMS current required 2.7 W of power. At 1 kHz, 6.8 W was required, because the impedance was reactance dominated at such frequencies.

The response of both the ferrofluid and air-filled actuators to frequency sweep signals were nearly independent of driving amplitude (<0.8 dB). Voltage-referenced frequency responses for each are shown in Fig. 5A (0 dB = 1 m/s^2/V). The air-filled actuator exhibits a resonance at 165 Hz (Q = 3.8), at which the measured peak-to-peak acceleration was 64.0 g at voltage amplitude 1.25 V (yielding current 0.2 A). As noted below, the air-filled actuator response was substantially non-linear at larger voltage values. In contrast, the ferrofluid actuator exhibited no resonance. The acceleration response of the ferrofluid actuator was resonance-free from 100 Hz to 1000 Hz, and remained substantially flat above 300 Hz. At frequencies below 40 Hz, acceleration was 6 dB larger in the ferrofluid device than it was in the air-filled actuator. At low frequencies, the peak unloaded accelerations of both actuators are displacement limited, thus explaining the rapid decline in acceleration response (Fig. 5A, inset).

When sinusoidally driven at frequencies below 50 Hz, the ferrofluid actuator displacements were substantial, reaching 1.6 mm at 1 A current (Fig. 5B). At high frequencies, peak-to-peak accelerations of the air-filled and ferrofluid actuators were similar: 20.0 g and 23.0 g respectively for a 750 Hz driving signal with amplitude 0.5 A.

The frequency-averaged THD of the ferrofluid actuator was −37 dB at 0.5 A. At 1 A, THD was less than −23 dB at all frequencies. In contrast, the air filled actuator response was nonlinear at moderate to high currents. The nonlinearity was most pronounced below the resonant frequency of 165 Hz. Mean THD for the air-filled actuator at 0.5 A was −15 dB for frequencies below 150 Hz, and −30 dB above 165 Hz.

In haptic applications involving compact actuators, transient performance is paramount. Duty cycles are often brief, since continuously sustained feedback sensations are often unpleasant. The ferrofluid actuator transient response was very fast. The unloaded rise time was 2 ms for a 0.5 A current step input that itself possessed a rise time of 1 ms. This elicited a peak acceleration of 4.7 g. This transient performance reflected the excellent bandwidth and damping characteristics of the ferrofluid actuator. In contrast, the air-filled actuator exhibited a slower rise time of 12 ms (Fig. 5C), due to the decreased damping and prominent 165 Hz resonance. The resonance resulted in a larger peak-to-peak acceleration of 19 g, as expected.

During brief transient operation, the ferrofluid actuator performance is not constrained by equilibrium thermal constraints, which require heat generated in the core to be radiated from the exterior surfaces. The thermal design of the actuator was sufficient to avoid heat concentration that might lead to thermal failure of the conductor or magnets. The actuator could repeatedly be driven by large, short duration current pulses as large as 38 Amperes (tested up to the current limit of our instrumentation), yielding transient forces as large as 12 N (Fig. 5E). Under repeated actuation, no loss in actuator performance was observed, underlining the effectiveness of the thermal design. Custom electronics could be designed to drive the actuator so as to produce larger forces. While such large currents cannot be sustained over longer periods, the ability of our design to handle repeated delivery large transient currents is an advantage in haptics applications.

During long duty cycle driving (yielding sustained forces), thermal effects become more pronounced, and the beneficial effects of heat distribution by the encapsulated ferrofluid again become apparent. When driven with a DC current of 1 A for 120 s, the temperature of the ferrofluid-filled actuator, measured at the base, increased by 13.5 C, while that of the air-filled actuator increased by 17.6 C. These measurements were, by design, very conservative, since they were captured with the actuator encased in an ABS fixture that insulated the exterior surfaces, greatly inhibiting radiative heat transfer.

The elastic reservoir that was port coupled to the actuator allowed us to investigate the extent to which the actuator response was sensitive to constraints arising from the incompressibility of the ferrofluid. When the reservoir size was varied by clamping (Fig. 6B), the acceleration response was virtually unchanged, varying by less than 1 dB across the range of tested frequencies (Fig. 6B). In other words, the actuator response is dominated by contributions of the membrane, moving masses, and other design features. A simpler, sealed port design (shown in Fig. 1B,D) is thus sufficient and recommended in practice.

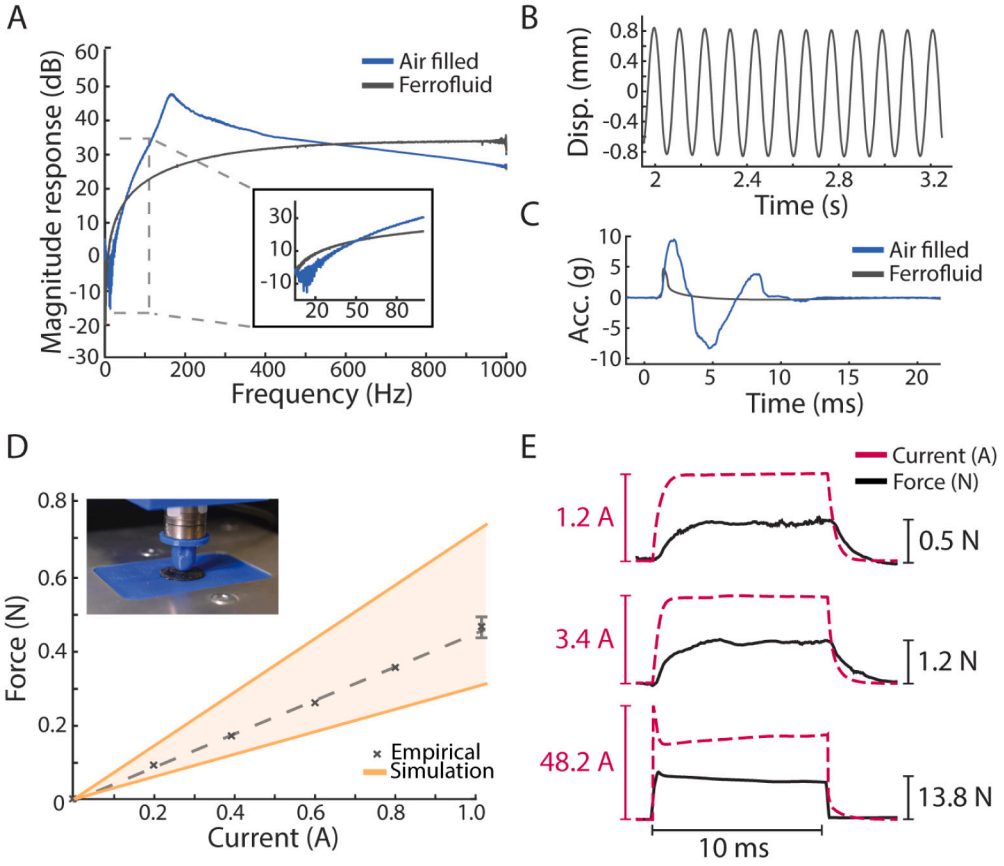

Fig. 5. (A) Voltage-specific acceleration frequency response for unloaded ferrofluid and air-filled actuators. 0 dB = 1 m/s^2/V, peak-to-peak. The air filled actuator exhibits a resonance at 165 Hz. The ferrofluid actuator exhibited no resonance. Both actuator responses were displacement limited at low frequencies. The ferrofluid actuator produced larger accelerations below 50 Hz, due to the greater magnetic permeability of ferrofluid compared to air. (B) Displacements of the moving mass of the ferrofluid actuator for an 8.5 Hz, 1 A amplitude sinusoidal current input. Peak displacements (800 μm) were consistent with predicted values from our analysis. (C) Step response of the actuators in response to a 0.5 A current step input. The longer rise time of the air filled actuator (12 ms) was due to its resonant characteristics. The ferrofluid actuator rise time was less than 2 ms. (D) Static forces produced by the ferrofluid actuator when driven with direct current (DC) from the midpoint of its stroke, reflecting a linear force–current relationship with slope 0.45 N/A. Error bars: standard deviation. Inset: actuator with measurement fixture and force transducer. (E) Forces as large as 13.8 N are produced in response to brief current pulses.

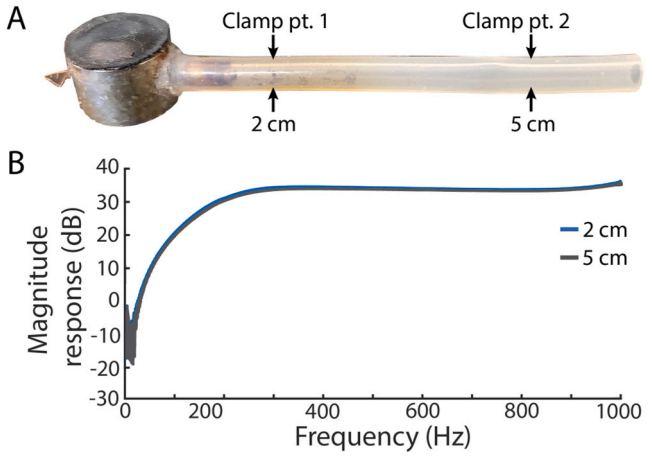

Fig. 6. Effects of fluid encapsulation on device dynamics were analyzed by porting otherwise closed volume of the ferrofluid filled actuator to an elastic tube. (A) The tube (Φ_{1D} = 3 mm) was clamped tightly to seal the system, with the resulting air column acting primarily as a spring. (B) The voltage-specific acceleration magnitude response (0 dB = 1 m/s^2/V, peak-to-peak) for different lengths of the air column (2 cm and 5 cm shown). No measurable difference was observed in the actuator response. Thus, a minimal, elastically sealed port design (shown in Fig. 1B,D) is adequate.

7.3. Discussion

The results show how this ferrofluid actuator design can reproduce controlled forces or displacements at frequencies from DC (constant forces) to 1000 Hz. The amplitude and phase response of the system were substantially linear for moderate driving voltages like those used in many haptics applications. The transient and steady-state response were free from resonant phenomena. Together, these attributes reflect the beneficial effects of ferrofluid on controlling actuator dynamics.

A comparison of the unloaded responses of the air-filled and ferrofluid actuators shows how the viscosity of the ferrofluid, and geometric features of the mechanism including the aluminium channel, impart significant damping. The resulting system is over-damped (calculated damping ratio $\zeta = 4$). This minimized effects of mechanical resonance on the dynamics of the system, as evidenced by the unloaded dynamic and step responses.

At low frequencies, the device is dominated by the stiffness and thus stiffness-limited in peak displacement. For electromagnetic forces F_{em}, the membrane does not displace more than F_{em}/k_{eff} from the equilibrium point. Fixed amplitude sinusoidal driving yielded accelerations that increase with frequency f

$$a = d^2z/dt^2 = (2\pi f)^2 z$$

At low frequencies below 40 Hz (Fig. 5A Inset), the measured accelerations increase with increasing frequency at the expected 40 dB/decade

Table 2
Comparative table of vibrotactile actuators.

	Constructed actuator	ERM	Haptuator Mk II	C-2 Tactor	LRA	Piezo
Volume, cm^3	3.4	0.27	5.2	1.5	0.3	1.6
Mass, grams	19.5	1.1	8.7	17	2	6.7
Operating freq., Hz	DC - 1000	167	90 - 1000	200 - 300	175	DC - 500
Stroke, mm	1.6	–	–	1	–	0.025
Static force, N	0.45	–	–	[a]	–	4.5
Peak-to-peak acceleration, g	46 (unloaded)	0.9	8	[a]	1.5	32
Power handling, W (freq., Hz)	2.7 (DC) >3 (100 to 1000) >3000 (10 ms pulse)	0.06 ([a])	0.3 (125)	1 (250)	0.046 (175)	[a]

[a]Indicates lack of publicly available data.

rate. At such frequencies, the fabricated actuator achieved peak-to-peak displacements of 1.6 mm when sinusoidally driven, drawing a peak-to-peak current of $I = 1$ A.

For signals that cause large unloaded displacements of the moving mass along the stroke, such as large current inputs at low frequencies, or around the resonance of the air-filled actuator, nonlinearities due to membrane hyperelasticity constrain the linear operating range of displacements. The effective stroke length was 1.25 mm in the linear regime, for which THD remained below −30 dB at all frequencies. This stroke length along with the very short rise and fall times (Fig. 5C) make it possible to use the actuator to deliver not only vibrations in sustained contact, but also to produce transient contact sensations, by configuring the device with a small gap to the skin. Such transient-contact haptic stimuli are very easily felt, due to the numerous highly sensitive vibration sensitive receptors in the skin, including Meissner corpuscle and Pacinian corpuscle touch receptors.

The optimized heat transport characteristics of the actuator augment power handling, enabling it to produce static forces of 0.45 N when supplied with 2.7 W of power (Fig. 5D). Practical haptic devices and applications rarely involve forces or vibrations with such long durations. Our results also indicate that currents as large as 6 A can be used for durations of at least 3 s without damage, yielding quasi-static forces of nearly 3 Newtons. Brief, 10 ms, current pulses as large as 38 A can also be used yielding transient forces of 12 N (Fig. 5E). Such driving signals can be repeatedly applied without causing damage. Together, the performance characteristics of this actuator compare favorably to those of similarly sized devices. Table 2 compiles performance characteristics for several commercially available haptic actuators. The table also permits the interested reader to compare the listed performance measures with the respective actuator volumes and masses. The force–current relationship was sub-linear for currents above 2 A, consistent with our theoretical analyses, due to effects of magnetic saturation. Nevertheless, these measurements highlight the large dynamic range that is achieved for time-varying signals matching the characteristics of how such devices are used in haptics.

The performance could be substantially improved by enhancing the magnetic permeability of the core materials through the use of standard annealing procedures that could not be fully reproduced using systems available to the authors. Nonetheless, the annealing we applied improved the saturation field strength of the actuator, aiding linearity and increasing the operating range of forces. We calculate, and our simulations suggest (Fig. 5D), that force output can be increased by 60% within the current design by further optimizing the metallurgy. The constructed actuator is unique among electromagnetic actuators in its ability to generate sustained (DC) forces, oscillating forces or displacements across a wide frequency bandwidth. As a further comparison, piezoelectric actuators can deliver comparable sensations in bipolar operation, but their utility is hampered by complex driving requirements, small displacements, and thermal constraints at high frequencies. In contrast, the ferrofluid electromagnetic actuator reported here can be driven through simple commodity electronics similar to those that are used in many consumer devices.

In configurations where the finger firmly applies a load to the actuator, the system is coupled to the dynamics of the skin. For small indentations, estimates for the stiffness of the fingertip volar skin range from 0.25 to 1 N/mm [49], which is moderately smaller than the driving point stiffness at the actuator membrane. Determining the effects of skin mechanics on the delivery of haptic stimuli requires analyses involving continuum contact mechanics, sensory neuroscience, and perception that would be beyond the scope of this article, but merit future investigation.

8. Conclusion

The ferrofluid-encapsulating electromagnetic actuator designs presented here are compact and meet requirements for delivering high-quality haptic feedback in regimes that are inaccessible to devices used in current practice. The actuators generate forces between permanent magnets and electromagnetic coils, and employ an elastic membrane to provide a restoring force to a moving mass at the output driving point. This design allows for a large operating bandwidth, from DC to 1000 Hz, enabling the delivery of vibrations through the entire tactile range of sensitivity of the skin. The actuators are capable of producing sustained forces up to 3 N and transient forces exceeding 12 N, making them suitable for providing a diverse range of haptic stimuli to the skin, including forces, indentations, and vibrations.

In addition to their impressive performance, these actuators are also compact in size and thus may be suitable for integration into handheld interfaces, instruments, and wearable devices. The enclosing surfaces shield the magnetic flux produced by the actuator, making them compatible with applications in complex haptic systems that integrate arrays of multiple actuators positioned in close proximity to each other or to other electronics. The actuator designs reported here could advance haptic technologies and applications in areas ranging from augmented and virtual reality, to mobile and wearable computing, and robotic teleoperation.

CRediT authorship contribution statement

Nikolas Kastor: Fabricated the actuators, Designed the actuator and performed theoretical and numerical modeling, Performed measurements and analyses. **Bharat Dandu:** Designed the actuator and performed theoretical and numerical modeling, Performed measurements and analyses. **Vedad Bassari:** Designed the actuator and performed theoretical and numerical modeling, Performed measurements and analyses. **Gregory Reardon:** Performed measurements and analyses. **Yon Visell:** Designed the actuator and performed theoretical and numerical modeling, Supervised the work and provided reagents and resources.

Declaration of competing interest

The authors declare that they have no known competing financial interests or personal relationships that could have appeared to influence the work reported in this paper.

Data availability

Data will be made available on request.

Acknowledgments

The authors thank Dano Pagenkopf, Dr. Amanda Strom, and Andy Weinberg for their assistance. We acknowledge the use of the UCSB Material Research Laboratory facilities (NSF DMR 1720256), and the UCSB Engineering Machine Shop. This work was supported by US National Science Foundation Award 1751348.

References

[1] S. Choi, K.J. Kuchenbecker, Vibrotactile display: Perception, technology, and applications, Proc. IEEE 101 (9) (2012) 2093–2104.
[2] W. Dangxiao, G. Yuan, L. Shiyi, Y. Zhang, X. Weiliang, X. Jing, Haptic display for virtual reality: progress and challenges, Virtual Real. Intell. Hardw. 1 (2) (2019) 136–162.
[3] F. Sorgini, R. Caliò, M.C. Carrozza, C.M. Oddo, Haptic-assistive technologies for audition and vision sensory disabilities, Disabil. Rehabil. Assist. Technol. 13 (4) (2018) 394–421.
[4] L.A. Jones, Haptics, MIT Press Essential Knowledge series, 2018.
[5] S. Biswas, Y. Visell, Emerging material technologies for haptics, Adv. Mater. Technol. 4 (4) (2019) 1900042.
[6] S. Biswas, Y. Visell, Haptic perception, mechanics, and material technologies for virtual reality, Adv. Funct. Mater. (2021) 2008186.
[7] D.W. Weir, M.A. Peshkin, J.E. Colgate, P. Buttolo, Design and performance of a high fidelity, low mass, linear haptic display, in: First Joint Eurohaptics Conference and Symposium on Haptic Interfaces for Virtual Environment and Teleoperator Systems. World Haptics Conference, IEEE, 2005, pp. 177–182.
[8] W. McMahan, K.J. Kuchenbecker, Dynamic modeling and control of voice-coil actuators for high-fidelity display of haptic vibrations, in: 2014 IEEE Haptics Symposium, HAPTICS, IEEE, 2014, pp. 115–122.
[9] G. Korres, M. Eid, Design of low-profile tactile actuator with rich vibrotactile stimulation for wearable applications, in: 2019 IEEE International Symposium on Haptic, Audio and Visual Environments and Games, HAVE, IEEE, 2019, pp. 1–6.
[10] P. Preechayasomboon, A. Israr, M. Samad, Chasm: A screw based expressive compact haptic actuator, in: Proceedings of the 2020 CHI Conference on Human Factors in Computing Systems, 2020, pp. 1–13.
[11] H.-Y. Yao, V. Hayward, Design and analysis of a recoil-type vibrotactile transducer, J. Acoust. Soc. Am. 128 (2) (2010) 619–627.
[12] V. Hayward, K.E. MacLean, Do it yourself haptics: part i, IEEE Robot. Autom. Mag. 14 (4) (2007) 88–104.
[13] J.J. Zárate, H. Shea, Using pot-magnets to enable stable and scalable electromagnetic tactile displays, IEEE Trans. Haptics 10 (1) (2016) 106–112.
[14] F. Pece, J.J. Zarate, V. Vechev, N. Besse, O. Gudozhnik, H. Shea, O. Hilliges, MagTics: Flexible and thin form factor magnetic actuators for dynamic and wearable haptic feedback, in: Proceedings of the 30th Annual ACM Symposium on User Interface Software and Technology, 2017, pp. 143–154.
[15] H. Boys, G. Frediani, S. Poslad, J. Busfield, F. Carpi, A dielectric elastomer actuator-based tactile display for multiple fingertip interaction with virtual soft bodies, in: Electroactive Polymer Actuators and Devices (EAPAD) 2017, vol. 10163, International Society for Optics and Photonics, 2017, p. 101632D.
[16] J.-H. Youn, H. Mun, K.-U. Kyung, A wearable soft tactile actuator with high output force for fingertip interaction, IEEE Access 9 (2021) 30206–30215.
[17] A. Israr, S. Zhao, K. Schwalje, R. Klatzky, J. Lehman, Feel effects: enriching storytelling with haptic feedback, ACM Trans. Appl. Perception (TAP) 11 (3) (2014) 1–17.
[18] S.A. Macdonald, S. Brewster, F. Pollick, Eliciting emotion with vibrotactile stimuli evocative of real-world sensations, in: Proceedings of the 2020 International Conference on Multimodal Interaction, 2020, pp. 125–133.
[19] B. Dandu, Y. Shao, Y. Visell, Rendering spatiotemporal haptic effects via the physics of waves in the skin, IEEE Trans. Haptics 14 (2) (2020) 347–358.
[20] A. Kawazoe, G. Reardon, E. Woo, M. Di Luca, Y. Visell, Tactile echoes: Multisensory augmented reality for the hand, IEEE Trans. Haptics (2021).
[21] A. Ghosh, B. Corves, Introduction to Micromechanisms and Microactuators, Springer, 2015.
[22] K. Raj, R. Moskowitz, Commercial applications of ferrofluids, J. Magn. Magn. Mater. 85 (1–3) (1990) 233–245.
[23] R.E. Rosensweig, Y. Hirota, S. Tsuda, K. Raj, Study of audio speakers containing ferrofluid, J. Phys.: Condens. Matter 20 (20) (2008) 204147.
[24] E. Uhlmann, N. Bayat, High precision positioning with ferrofluids as an active medium, CIRP Ann. 55 (1) (2006) 415–418.
[25] J.-H. Lee, Y.-J. Nam, M.-K. Park, Magnetic fluid actuator based on passive levitation phenomenon, J. Intell. Mater. Syst. Struct. 22 (3) (2011) 283–290.
[26] R. Olaru, C. Petrescu, R. Hertanu, A novel double-action actuator based on ferrofluid and permanent magnets, J. Intell. Mater. Syst. Struct. 23 (14) (2012) 1623–1630.
[27] L. Nascutiu, Voice coil actuator for hydraulic servo valves with high transient performances, in: 2006 IEEE International Conference on Automation, Quality and Testing, Robotics, 1, IEEE, 2006, pp. 185–190.
[28] M.-M. Mihai, A. Arcire, R. Olaru, Vibration mini actuator with magnetically suspended inertial mass, in: 2016 International Conference and Exposition on Electrical and Power Engineering, EPE, IEEE, 2016, pp. 083–086.
[29] T. Hulin, M. Rothammer, I. Tannert, S. Subramanyam Giri, B. Pleintinger, H. Singh, B. Weber, C. Ott, FingerTac–A wearable tactile thimble for mobile haptic augmented reality applications, in: International Conference on Human-Computer Interaction, Springer, 2020, pp. 286–298.
[30] C.-H. Kuo, S. Smith, Mechanical feedback analysis of a ferrofluid-based module with 2D dynamic traveling waves for tactile display application, Displays 61 (2020) 101926.
[31] L. Vaidman, Torque and force on a magnetic dipole, Amer. J. Phys. 58 (10) (1990) 978–983.
[32] J.J. Zárate, G. Tosolini, S. Petroni, M. De Vittorio, H. Shea, Optimization of the force and power consumption of a microfabricated magnetic actuator, Sensors Actuators A 234 (2015) 57–64.
[33] D. Vokoun, M. Beleggia, L. Heller, P. Šittner, Magnetostatic interactions and forces between cylindrical permanent magnets, J. Magn. Magn. Mater. 321 (22) (2009) 3758–3763.
[34] M. Kwon, J. Jung, T. Jang, S. Sohn, Magnetic forces between a magnet and a solenoid, Phys. Teacher 58 (5) (2020) 330–334.
[35] D. Giovanni, Flat and Corrugated Diaphragm Design Handbook, Routledge, 2017.
[36] Y. Visell, J.R. Cooperstock, Design of a vibrotactile display via a rigid surface, in: 2010 IEEE Haptics Symposium, IEEE, 2010, pp. 133–140.
[37] A. Zeaiter, M. Fénot, D. Saury, Numerical approach to determining windings' thermal conductivity, in: 2018 XIII International Conference on Electrical Machines, ICEM, 2018, pp. 1291–1296, http://dx.doi.org/10.1109/ICELMACH.2018.8506692.
[38] W. Zhao, X. Wang, S. Wu, S. Cui, C. Gerada, H. Yan, Eddy current losses analysis and optimization design of litz-wire windings for air-core compulsators, IEEE Trans. Plasma Sci. 47 (5) (2019) 2532–2538.
[39] Permalloy 80 technical data, 1999.
[40] Carpenter HyMu 80 datasheet, 2015.
[41] Ndfeb magnets/neodymium iron boron magnets datasheet, 2021.
[42] Sintered Neodymium-Iron-Boron Magnets Datasheet, Rev. 210607, 2017.
[43] Thermally conductive epoxy encapsulating and potting compound 832TC, technical data sheet, 2016.
[44] Duralco thermally conductive epoxy datasheet, 2021.
[45] Thermal properties of plastic materials, 2021.
[46] M. Higano, A. Miyagawa, K. Saigou, H. Masuda, H. Miyashita, Measuring the specific heat capacity of magnetic fluids using a differential scanning calorimeter, Int. J. Thermophys. 20 (1) (1999) 207–215, http://dx.doi.org/10.1023/a:1021498701969.
[47] M. Goharkhah, S. Gharehkhani, S. Fallah, M. Ashjaee, Dynamic measurement of ferrofluid thermal conductivity under an external magnetic fieldr, Heat Mass Transf. 55 (2019) 1583–1592.
[48] M. Amjadi, Y.J. Yoon, I. Park, Ultra-stretchable and skin-mountable strain sensors using carbon nanotubes–Ecoflex nanocomposites, Nanotechnology 26 (37) (2015) 375501.
[49] J. Park, N. Pažin, J. Friedman, V.M. Zatsiorsky, M.L. Latash, Mechanical properties of the human hand digits: Age-related differences, Clin. Biomech. 29 (2) (2014) 129–137.